VIP Energy Storage Materials Very Important Paper

Deutsche Ausgabe: DOI: 10.1002/ange.201602631
Internationale Ausgabe: DOI: 10.1002/anie.201602631

Dual-Doped Molybdenum Trioxide Nanowires: A Bifunctional Anode for Fiber-Shaped Asymmetric Supercapacitors and Microbial Fuel Cells

Minghao Yu, Xinyu Cheng, Yinxiang Zeng, Zilong Wang, Yexiang Tong, Xihong Lu, and Shihe Yang**

Abstract: *A novel in situ N and low-valence-state Mo dual doping strategy was employed to significantly improve the conductivity, active-site accessibility, and electrochemical stability of MoO_3, drastically boosting its electrochemical properties. Consequently, our optimized N-MoO_{3-x} nanowires exhibited exceptional performances as a bifunctional anode material for both fiber-shaped asymmetric supercapacitors (ASCs) and microbial fuel cells (MFCs). The flexible fiber-shaped ASC and MFC device based on the N-MoO_{3-x} anode could deliver an unprecedentedly high energy density of 2.29 mWh cm^{-3} and a remarkable power density of 0.76 μW cm^{-1}, respectively. Such a bifunctional fiber-shaped N-MoO_{3-x} electrode opens the way to integrate the electricity generation and storage for self-powered sources.*

Modern electronics is trending toward tiny, lightweight and portable vogues to suit specific environments.[1] In particular, wearable electronic commodities represent a crucial advance due to their enormous application potentials in highly integrated and on-body equipment.[2] To power these electronics in wearable systems, flexible lightweight fiber-shaped energy devices are indispensable.[3] As a promising sustainable technology, particularly in terms of the feasibility for wastewater treatment,[4] microbial fuel cells (MFCs) can directly generate electricity from biodegradable organic compounds with bacteria. Nevertheless, virtually no study has been reported on the construction of flexible fiber-shaped MFC devices. When it comes to energy storage, asymmetric supercapacitors (ASCs) are of particular interest, which are featured by their fast charge/discharge abilities and ultralong cycling lifetime.[5] Despite the impressive developments of MFCs and fiber-shaped supercapacitors,[6] further breakthroughs in electrode materials are required to fulfill the critical demands for high output power density of MFCs and high energy density of ASCs, especially in anode materials.[7]

Molybdenum trioxide (MoO_3) is an excellent electrode material for its low cost, multiple valence states of Mo, and environmentally benign nature.[8] In particular, MoO_3 has a considerably high work function (6.9 eV),[8c] lending a wider operation potential window for ASCs determined by the difference of electrode pair work functions. Unfortunately, because of the poor conductivity of MoO_3 (ca. 10^{-5} S cm^{-1}), most of the current MoO_3 based electrodes were plagued by the sluggish faradaic redox kinetics, insufficient rate capability, and rapid degradation of performance.[8] It remains a vital issue to fundamentally ameliorate these issues.

Herein, we firstly demonstrated a new in situ N and low-valence-state Mo dual doping strategy that remarkably boosted the electrochemical performance of MoO_3 nanowires and their implementations as bifunctional anodes for both ASCs and MFCs. Owing to the strengthened Mo–Mo bond in MoO_{3-x} ($x < 3$), the introduction of low-valence-state Mo into MoO_3 could not only improve its conductivity, but also provide more active sites for electrochemical reactions.[9] Meanwhile, nitrogen doping has been proved to effectively tailor electrical, mechanical and surface properties of metal oxides.[10] Drawing on these, we have prepared free-standing N-doped MoO_{3-x} (denoted as N-MoO_{3-x}) nanowires with a highly open structure, rough surface and superior hydrophilicity for easy electrolyte permeation by a simple thermal reduction process of MoO_3 nanowires in the NH_3 atmosphere. Impressively, the optimized N-MoO_{3-x} nanowires presented exceptional electrochemical performance as anode materials in both fiber-shaped ASCs and fiber-shaped MFCs.

Free-standing MoO_3 nanowires were firstly grown onto the surface of the carbon fibers via a facile hydrothermal method (see Figure S1 in the Supporting Information). To introduce low-valence-state Mo and N dopants, the as-prepared MoO_3 nanowires were thermally reduced under various temperatures ranging from 500 to 900 °C in NH_3 atmosphere. The scanning electron microscopy (SEM) images reveal the as-fabricated *N*-MoO_{3-x} nanowires under 700 °C well preserved the overall morphology of MoO_3 (Figure 1 a,b). When the thermal treatment temperature reached 900 °C, a slight structural collapse occurred (Figure S2). On comparing the transmission electron microscopy (TEM) images of MoO_3 (Figure S3) and N-MoO_{3-x} (Figure 1 c) samples, one notices that the smooth MoO_3 nanowire surface turned rough after thermal treatment. And the single-crystallites became polycrystalline revealed by the selected-

[*] M. H. Yu, X. Y. Cheng, Y. X. Zeng, Prof. Y. X. Tong, Prof. X. H. Lu
MOE of the Key Laboratory of Bioinorganic and Synthetic Chemistry, KLGHEI of Environment and Energy Chemistry, School of Chemistry and Chemical Engineering, Sun Yat-Sen University
Guangzhou 510275 (P.R. China)
E-mail: luxh6@mail.sysu.edu.cn
Z. L. Wang, Prof. S. H. Yang
Department of Chemistry, The Hong Kong University of Science and Technology
Clear Water Bay, Kowloon, Hong Kong (China)
E-mail: chsyang@ust.hk

Supporting information for this article can be found under: http://dx.doi.org/10.1002/anie.201602631.

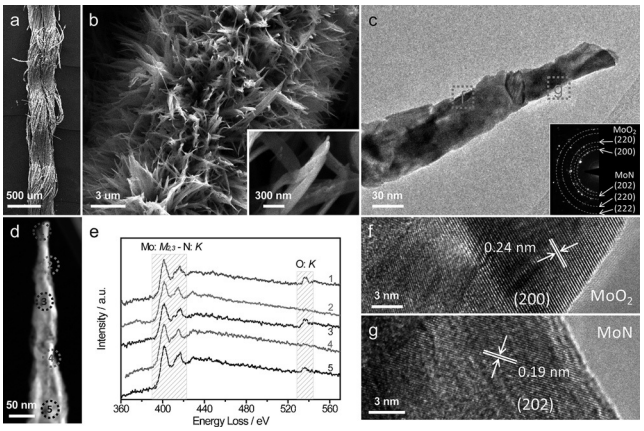

Figure 1. SEM images of (a) a bundle of N-MoO_{3-x}-coated carbon fibers, b) a N-MoO_{3-x}-coated carbon fiber fabricated under 700 °C. c) TEM image and d) HAADF-STEM image of a N-MoO_{3-x} nanowire. Inserted in (c) is its SAED pattern. e) EELS obtained from the circle areas in (d). f,g) HRTEM images obtained from the square areas in (c).

area electron diffraction (SAED) pattern (inset of Figure 1 c). The bright diffraction pattern obtained for N-MoO_{3-x} can be indexed to monoclinic MoO_2 (JCPDS = 65-5787) and hexagonal MoN (JCPDS = 25-1367). The high-angle annular dark-field scanning transmission electron microscope (HAADF-STEM) image of the single N-MoO_{3-x} nanowire also confirms the uneven surface (Figure 1 d). The electron energy loss spectroscopy (EELS) patterns at five selected sites on the nanowire are collected (Figure 1 e). The main features of these spectra include the O K-peaks centered at 536 eV, Mo $M_{2,3}$ doublet peaks spanning from 392 to 422 eV and N K-edges located at about 401 eV (overlapped with Mo M_3-peaks).[11] Both intensities and shapes of the O K-peaks vary from site to site, implying an inhomogeneous distribution of the O element. Similarly, the intensity ratios of Mo M_2 to Mo M_3-peaks and the peak shapes are also different, pointing to the heterostructure due to the partial reduction of MoO_3. High-resolution TEM (HRTEM) images (Figure 1 f and 1 g) also confirm the existence of crystalline MoO_2 and MoN. The observed lattice spacings of 0.24 nm and 0.19 nm correspond to the (200) plane of MoO_2 and (202) plane of MoN, respectively.

X-ray diffraction (XRD) analysis (Figure S4) was conducted for MoO_3 and N-MoO_{3-x} samples fabricated under 500, 600, 700, 800, and 900 °C (denoted as N-MoO_{3-x}-5, N-MoO_{3-x}-6, N-MoO_{3-x}-7, N-MoO_{3-x}-8, MoN, respectively). The original MoO_3 is readily indexed to hexagonal MoO_3 (JCPDS card no. 21-0569). As the thermal treatment temperature increased, most of MoO_3 peaks disappeared, accompanying with the appearance of MoO_2 (JCPDS card number 65-5787) and MoN (JCPDS card number 25-1367) peaks. When the temperature reached 900 °C, only the peaks of MoN were retained, indicating MoO_3 completely transformed into MoN. X-ray photoelectron spectroscopy (XPS) analysis was also performed. The O 1s peaks are observed to continually diminish with the increase of thermal treatment temperature, which meets the fact that MoO_3 is gradually reduced (Figure S5 a). Simultaneously, as for both Mo 3p 1/2 (Figure S5 b) and Mo 3d peaks (Figure S5 c), new peaks at lower binding energy with increasing intensities are observed, suggesting the valence state of Mo decreases. All N 1s–Mo $3p_{3/2}$ peaks could be de-convoluted into Mo $3p_{3/2}$ peaks of Mo^{6+} (399.3 eV),[12] Mo^{4+} (396.3 eV),[12] Mo^{3+} (394.9 eV),[13] and N 1s peaks (397.6 eV), respectively (Figure 2 a and S6). The calculated

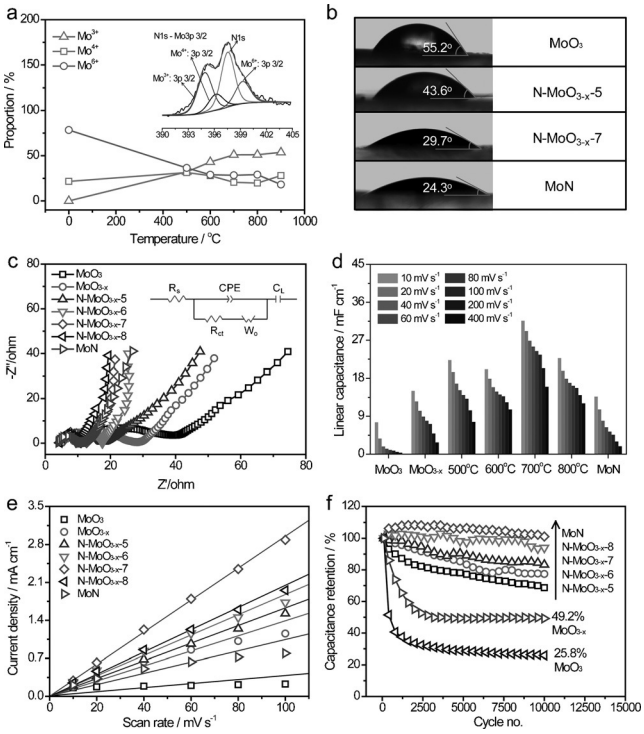

Figure 2. a) The proportions of Mo^{6+}, Mo^{4+} and Mo^{3+} in surface MoO_3 and N-MoO_{3-x} samples. The inset: core-level N 1s–Mo $3p_{3/2}$ XPS spectrum of N-MoO_{3-x}-7 sample. b) Contact angles of a water droplet on MoO_3 and N-MoO_{3-x} samples. c) EIS collected for all electrodes. Inserted in (c) is the equivalent circuit employed for fitting the EIS results. d) Linear capacitances of all electrodes at various scan rates. e) The anodic charging current densities measured at −0.5 V in CV curves as a function of the scan rate for all electrodes. f) Cycling performance obtained for all electrodes.

distributions of different molybdenum valence states are shown in Figure 2 a. Overall, the proportion of Mo^{6+} undergoes a downward trend, while an opposite trend was observed for that of Mo^{3+}, and the proportion of Mo^{4+} fluctuates. Besides, the element contents of Mo, O, and N for these samples are listed in Table S1, which accord with the trend of Mo valences. For electrode materials, hydrophilicity is of great significance for allowing an efficient access of the ions to the electrode/electrolyte interface. As expected, the water contact angles of N-MoO_{3-x} samples gradually decrease from 55.2° to 24.3° with increasing annealing temperature (Figure 2 b), demonstrating that the wettability can be significantly enhanced after low-valence-state Mo and N doping.

We next turn to electrochemical impedance spectroscopy (EIS) to examine the effect of two dopants on the kinetics of ionic and charge transport in the electrodes (Figure 2 c). EIS

of only low-valence-state Mo-doped MoO_3 electrode (denoted as MoO_{3-x}, Figure S7) was also conducted. The results were analyzed with the equivalent circuit (inset of Figure 2c), and the fitting results are summarized in Table S2. As reflected by the diminished charge-transfer resistance (R_{ct}) and enhanced limited capacitance (C_L) of MoO_{3-x} (16.30 Ω, 0.003 F) in comparison with MoO_3 (30.97 Ω, 10×10^{-7} F), the introduction of low-valence-state Mo could efficiently improve the electronical conductivity and capacitive activity. Similarly, the doped N was also demonstrated to offer superior charge transfer ability with a small R_{ct} of MoN (3.16 Ω). The linear resistivities of all electrodes are shown in Figure S8, which is consistent with the trend of R_{ct}. All these results confirmed our hypothesis that electrical conductivity, ionic diffusion rate, and capacitive activity of the MoO_3 electrode can be enhanced by the co-doping with N and low-valence-state Mo.

Figure 2d further illustrates the linear capacitance of MoO_3, MoO_{3-x} and N-MoO_{3-x} electrodes, which are extracted from their cyclic voltammetry (CV) profiles (Figure S7d and S9). The linear capacitances of all dual-doped N-MoO_{3-x} electrodes obviously outperform those of MoO_3, mono-doped MoO_{3-x} and MoN electrodes at all the scan rates, and the N-MoO_{3-x}-7 electrode yielded the highest capacitance. For example, the N-MoO_{3-x}-7 achieved a remarkable linear capacitance of 31.6 mF cm^{-1} (25.3 F cm^{-3}), while the corresponding linear capacitances of MoO_3, MoO_{3-x}, N-MoO_{3-x}-5, N-MoO_{3-x}-6, N-MoO_{3-x}-8, and MoN are 7.6, 15.0, 22.3, 20.2, 22.7 and 13.7 mF cm^{-1}, respectively. Moreover, this high linear capacitance of N-MoO_{3-x}-7 outperforms most of recently reported fiber-shaped electrodes.[6a,e,f] Its outstanding electrochemical performance is also evidenced by its substantially longer discharge time in the galvanostatic charge/discharge (GCD) curves (Figures S10 and S11). Electrochemically active surface area was estimated using a mature method widely utilized in oxygen evolution reaction catalyst (SI).[14] Figure 2e displays anodic charging current densities (I) measured at −0.5 V as a function of the scan rate (v) for all electrodes. Importantly, the N-MoO_{3-x}-7 sample achieved the steepest slope, revealing that it possesses the largest electrochemically active surface area. In addition, the long-term stability of the MoO_3, MoO_{3-x} and N-MoO_{3-x} electrodes were also evaluated (Figure 2f). Specifically, the MoN electrode owns the best cycling performance with nearly no capacitance decay after 10000 cycles, whereas 6.1%, 16.7%, 22.6%, and 31.3% capacitance decline occurred to the N-MoO_{3-x}-8, N-MoO_{3-x}-7, N-MoO_{3-x}-6, and N-MoO_{3-x}-5 electrodes, respectively. This result convincingly confirms that the N dopant plays the dominant role in stabilizing the MoO_3 electrode. Taken together, the N-MoO_{3-x}-7 electrode shows the optimized performance, which is ascribed to the combined effects of the remarkably improved conductivity, enhanced surface wettability, fast ionic diffusion rate, increased active sites, and chemical inertness as a result from the introduction of appropriate N and low-valence-state Mo.

A fiber-shaped solid-state ASC device (denoted as MnO_2@TiN//N-MoO_{3-x}-ASC) made up of a N-MoO_{3-x}-7 anode and a mature MnO_2@TiN cathode (Figure S12 and S13) was illustrated in Figure 3a. GCD curves of MnO_2@TiN//N-MoO_{3-x}-ASC device with different operation windows imply a suitable operating potential of 2.0 V (Figure S14). The nearly triangular shapes of all GCD curves (Figure 3b) with similar shapes reveal its ideal capacitive characteristics. More importantly, the maximum linear and volumetric capacitances of MnO_2@TiN//N-MoO_{3-x}-ASC device are calculated to be 10.3 mF cm^{-1} and 4.1 F cm^{-3} at 0.25 mA cm^{-1} (Figure 3c), respectively. When the current density increased by 15 folds, a large linear capacitance of 4.9 mF cm^{-1} (2.0 F cm^{-3}) was still retained. CV curves of our ASC device under normal, bent, and knotted conditions were collected in Figure 3d. No variation from these CV curves were observed, even at knotted state, which indicates the fiber-shaped ASC device has prominent flexibility that could stably perform under different levels of deformation. In addition, Figure 3e compares the energy densities and power densities of our ASC device with the recently reported ASC devices. Notably, our MnO_2@TiN//N-MoO_{3-x}-ASC device delivered a maximum energy density of 2.29 mWh cm^{-3} with a slow discharge time of 81.7 s. As a quantitative comparison, this remarkable energy density is considerably higher than recently reported fiber-shaped SC devices.[6a–d,g,h] The

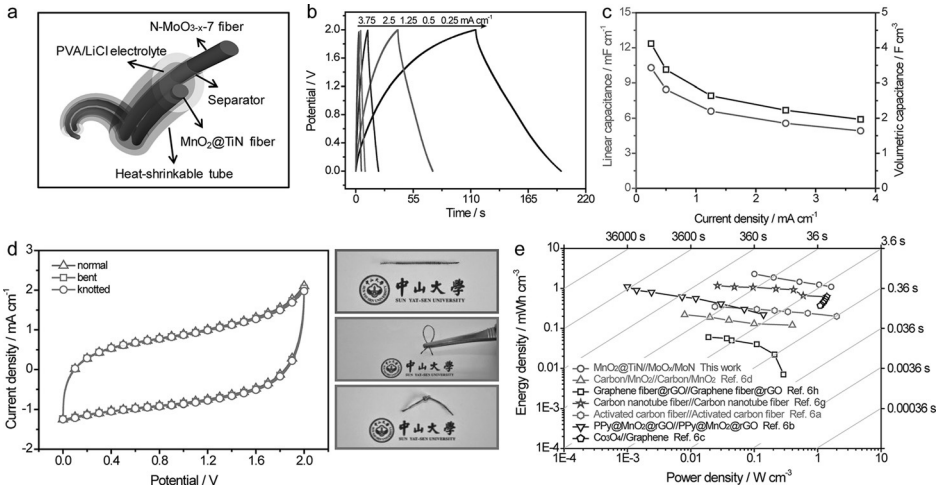

Figure 3. a) Schematic illustration of the as-assembled fiber-shaped MnO_2@TiN//N-MoO_{3-x}-ASC device. b) GCD curves of our fiber-shaped ASC device. c) Linear capacitances and volumetric capacitances of the fiber-shaped ASC device as a function of current density. d) CV curves collected at 100 mV s^{-1} for the fiber-shaped ASC device under different conditions (left) and corresponding device pictures (right). e) Ragone plots for the fiber-shaped ASC device and other recently reported fiber-shaped SCs.[6a–d,g,h]

obtained power densities of our ASC device also outperform those of reported fiber-shaped SC devices at similar discharge times. The maximum power density of our device reached 1.64 $W\,cm^{-3}$ when it was operated at a short discharge time of 2.4 s. Simultaneously, our fiber-shaped ASC device showed good stability with 80.3% of its initial capacitance was retained after 5000 charge/discharge cycles at 100 $mV\,s^{-1}$ (Figure S15).

The optimized N-MoO_{3-x} electrode was further employed as anode to construct an Escherichia coli cell catalyzed MFC device with fiber-shaped architecture (denoted as Pt/C//N-MoO_{3-x}-MFC). To the best of our knowledge, this is the first attempt to construct MFC device with a fiber-shaped configuration. Figure 4a shows the schematic illustration of the as-assembled fiber-shaped MFC device. The polarization and power curves were recorded for Pt/C//N-MoO_{3-x}-MFC under both flat and bent conditions (Figure 4b). When it performed in a flat condition, it output the maximum power density of 0.76 $\mu W\,cm^{-1}$ (0.61 $mW\,cm^{-3}$) at a current density of 4.4 $\mu A\,cm^{-1}$. For better comparison, another similar MFC device was assembled by using pristine carbon fiber bundle as anode, which is one of the most commercial MFC anodes. By contrast, the maximum power density of the MFC device based on carbon fabric anode only reached 0.006 $\mu W\,cm^{-1}$ (Figure S16), which is two orders of magnitude less than that of Pt/C//N-MoO_{3-x}-MFC device, demonstrating the superior performance of N-MoO_{3-x} electrode as MFC anode. Moreover, the Pt/C//N-MoO_{3-x}-MFC device exhibited almost unchangeable polarization and power curves when tested at bent condition. Figure 4c displays two consecutive deeding cycles, each of which lasted for about 40–50 hours. The slow decay of power density was mainly due to the depletion of nutrients in anolyte, and once the anolyte was replenished, the power generation immediately restored. This demonstrated the fascinating promise of Pt/C//N-MoO_{3-x}-MFC to operate for a long period with continuous supply of organic nutrients. Finally, motivated by the general trend of self-sustained energy devices, we attempt to integrate our MnO_2//N-MoO_{3-x}-ASC device with Pt/C//N-MoO_{3-x}-MFC device to simultaneously realize the energy conversion from chemical energy to electricity and storage in ASC device (Figure S17). It is clearly shown that the ASC device could be charged to 0.15, 0.35, and 0.88 V by one, three and nine MFC devices after 150 s (Figure 4d). The charge mode of ASC device by MFCs was similar to constant potential charging method, and thus the ASC device could be charged to a high voltage rapidly by nine MFC devices. Such combination is believed to hold great promise as self-powered energy device to power wearable electronics in practical applications.

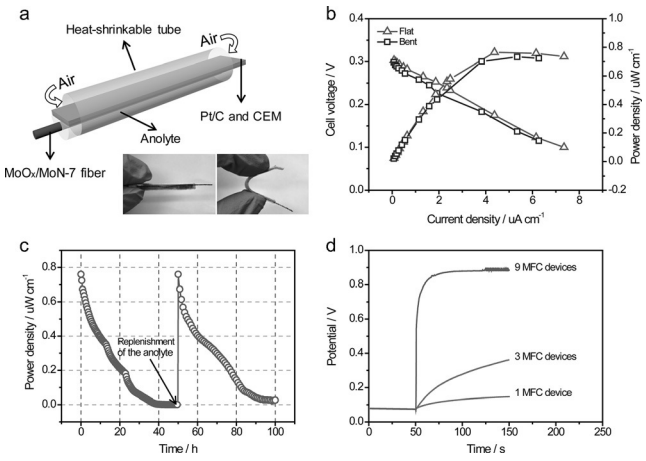

Figure 4. a) Schematic illustration of the as-assembled fiber-shaped MFC device. b) Polarization and power curves collected from a Pt/C//N-MoO_{3-x}-MFC device under both flat and bent conditions. c) Power density versus time plot collected for Pt/C//N-MoO_{3-x}-MFC device. d) Charging curves obtained for as-assembled ASC device by different numbers of our fiber-shaped MFC devices.

In summary, we have developed a facile and effective thermal reduction approach to codope MoO_3 nanowires and to significantly improve the electrochemical performance of the doped MoO_3 nanowires as promising bifunctional anodes in fiber-shaped ASCs and MFCs. Upon thermal treatment in NH_3, low-valence-state Mo and N dopants were successfully introduced into MoO_3 nanowires, endowing the N-Mo_{3-x} nanowires with high electrolyte accessibility enabled by the superior hydrophilicity, high conductivity and rich active sites. When the N-MoO_{3-x} nanowires obtained at 700 °C were used as anode, the as-fabricated ASC device achieved an extraordinary energy density of 2.29 $mWh\,cm^{-3}$ and power density of 1.64 $W\,cm^{-3}$. Further, a high-performance fiber-shaped MFC device based on the optimized N-MoO_{3-x} nanowires anode was firstly constructed. This fiber-shaped MFC device not only has excellent mechanical flexibility, but also could yield a remarkable power density of 0.76 $\mu W\,cm^{-1}$ and ultralong durability. The in situ low-valence-state Mo and N dual doping strategy developed here holds a great potential for boosting the electrochemical performances of other metal oxides, and the demonstration of using the same anode material in energy conversion and storage devices heralds new opportunities in the development of self-powered integrated devices.

Acknowledgements

We acknowledge the financial support of this work received by the Natural Science Foundation of China (grant numbers 21403306, 2141101037, and 21273290), NSFC/RGC Joint Research Scheme (grant number N HKUST610/14). Guangdong Natural Science Funds for Distinguished Young Scholar (grant number 2014A030306048), Technology Planning Project of Guangdong Province (grant number 2015B090927007) and the Fundamental Research Foundations for the Central Universities (grant number 15lgpy24).

Keywords: energy conversion · energy storage · fuel cells · molybdenum · supercapacitors

How to cite: *Angew. Chem. Int. Ed.* **2016**, *55*, 6762–6766
Angew. Chem. **2016**, *128*, 6874–6878

[1] a) J. Chmiola, C. Largeot, P. L. Taberna, P. Simon, Y. Gogotsi, *Science* **2010**, *328*, 480 – 483; b) W. Wang, W. Liu, Y. Zeng, Y. Han, M. Yu, X. Lu, Y. Tong, *Adv. Mater.* **2015**, *27*, 3572 – 3578.

[2] a) J. Xiao, L. Wan, S. Yang, F. Xiao, S. Wang, *Nano Lett.* **2014**, *14*, 831 – 838; b) Z. Yang, J. Deng, X. Chen, J. Ren, H. Peng, *Angew. Chem. Int. Ed.* **2013**, *52*, 13453 – 13457; *Angew. Chem.* **2013**, *125*, 13695 – 13699.

[3] a) L. Qiu, J. Deng, X. Lu, Z. Yang, H. Peng, *Angew. Chem. Int. Ed.* **2014**, *53*, 10425 – 10428; *Angew. Chem.* **2014**, *126*, 10593 – 10596; b) J. Bae, Y. J. Park, M. Lee, S. N. Cha, Y. J. Choi, C. S. Lee, J. M. Kim, Z. L. Wang, *Adv. Mater.* **2011**, *23*, 3446 – 3449.

[4] a) H. Wang, F. Qian, G. Wang, Y. Jiao, Z. He, Y. Li, *ACS Nano* **2013**, *7*, 8728 – 8735; b) H. Wang, F. Qian, Y. Li, *Nano Energy* **2014**, *8*, 264 – 273.

[5] a) Z. Yu, J. Thomas, *Adv. Mater.* **2014**, *26*, 4279 – 4285; b) C. Zhu, P. Yang, D. Chao, X. Wang, X. Zhang, S. Chen, B. K. Tay, H. Huang, H. Zhang, W. Mai, H. J. Fan, *Adv. Mater.* **2015**, *27*, 4566 – 4571.

[6] a) D. Yu, S. Zhai, W. Jiang, K. Goh, L. Wei, X. Chen, R. Jiang, Y. Chen, *Adv. Mater.* **2015**, *27*, 4895 – 4901; b) Y. Huang, H. Hu, Y. Huang, M. Zhu, W. Meng, C. Liu, Z. Pei, C. Hao, Z. Wang, C. Zhi, *ACS Nano* **2015**, *9*, 4766 – 4775; c) X. Wang, B. Liu, R. Liu, Q. Wang, X. Hou, D. Chen, R. Wang, G. Shen, *Angew. Chem. Int. Ed.* **2014**, *53*, 1849 – 1853; *Angew. Chem.* **2014**, *126*, 1880 – 1884; d) X. Xiao, T. Li, P. Yang, Y. Gao, H. Jin, W. Ni, W. Zhan, X. Zhang, Y. Cao, J. Zhong, L. Gong, W. C. Yen, W. Mai, J. Chen, K. Huo, Y. L. Chueh, Z. L. Wang, J. Zhou, *ACS Nano* **2012**, *6*, 9200 – 9206; e) D. Yu, K. Goh, Q. Zhang, L. Wei, H. Wang, W. Jiang, Y. Chen, *Adv. Mater.* **2014**, *26*, 6790 – 6797; f) V. T. Le, H. Kim, A. Ghosh, J. Kim, J. Chang, Q. A. Vu, D. T. Pham, J. H. Lee, S. W. Kim, Y. H. Lee, *ACS Nano* **2013**, *7*, 5940 – 5947; g) P. Xu, T. Gu, Z. Cao, B. Wei, J. Yu, F. Li, J.-H. Byun, W. Lu, Q. Li, T.-W. Chou, *Adv. Energy Mater.* **2014**, *4*, 1300759; h) Y. Meng, Y. Zhao, C. Hu, H. Cheng, Y. Hu, Z. Zhang, G. Shi, L. Qu, *Adv. Mater.* **2013**, *25*, 2326 – 2331.

[7] a) J. Jiang, Y. Li, J. Liu, X. Huang, C. Yuan, X. W. Lou, *Adv. Mater.* **2012**, *24*, 5166 – 5180; b) X. Xia, D. Chao, Z. Fan, C. Guan, X. Cao, H. Zhang, H. J. Fan, *Nano Lett.* **2014**, *14*, 1651 – 1658.

[8] a) X. Zhang, X. Zeng, M. Yang, Y. Qi, *ACS Appl. Mater. Interfaces* **2014**, *6*, 1125 – 1130; b) X. Cao, B. Zheng, W. Shi, J. Yang, Z. Fan, Z. Luo, X. Rui, B. Chen, Q. Yan, H. Zhang, *Adv. Mater.* **2015**, *27*, 4695 – 4701; c) J. Chang, M. Jin, F. Yao, T. H. Kim, V. T. Le, H. Yue, F. Gunes, B. Li, A. Ghosh, S. Xie, Y. H. Lee, *Adv. Funct. Mater.* **2013**, *23*, 5074 – 5083.

[9] a) K. M. Hercule, Q. Wei, A. M. Khan, Y. Zhao, X. Tian, L. Mai, *Nano Lett.* **2013**, *13*, 5685 – 5691; b) Y. Sun, X. Hu, J. C. Yu, Q. Li, W. Luo, L. Yuan, W. Zhang, Y. Huang, *Energy Environ. Sci.* **2011**, *4*, 2870.

[10] M. Yu, Y. Han, X. Cheng, L. Hu, Y. Zeng, M. Chen, F. Cheng, X. Lu, Y. Tong, *Adv. Mater.* **2015**, *27*, 3085 – 3091.

[11] a) D. Wang, D. S. Su, R. Schlögl, *Z. Anorg. Allg. Chem.* **2004**, *630*, 1007 – 1014; b) D. S. Su, *Anal. Bioanal. Chem.* **2002**, *374*, 732 – 735.

[12] T. A. Patterson, J. C. Carver, D. E. Leyden, D. M. Hercules, *J. Phys. Chem.* **1976**, *80*, 1700 – 1708.

[13] R. Sanjinés, C. Wiemer, J. Almeida, F. Lévy, *Thin Solid Films* **1996**, *290*, 334 – 338.

[14] C. C. McCrory, S. Jung, J. C. Peters, T. F. Jaramillo, *J. Am. Chem. Soc.* **2013**, *135*, 16977 – 16987.

Received: March 15, 2016
Published online: April 21, 2016

